Supporting Information

Diboron- and digermanium-doped dihydrodibenzohexacenes: Ge–B exchange to access boron-doped extended acenes

Heechan Kim,[a] Laura F. Peña,[b,c] Adrian Espineira-Gutierrez,[b,c] Carlos Romero-Nieto,*[b,c] and Robert J. Gilliard, Jr.*[a]

[a] *Department of Chemistry, Massachusetts Institute of Technology, Cambridge, Massachusetts 02139-4307, United States*
[b] *Faculty of Pharmacy, University of Castilla-La Mancha, Calle Almansa 14 - Edif. Bioincubadora, 02008, Albacete, Spain;*
[c] *Instituto Regional de Investigación Científica Aplicada (IRICA), University of Castilla−La Mancha, 13071 Ciudad Real, Spain*

Table of Contents **Pages**

1. General Procedures

All air- and moisture-sensitive reactions were carried out under an inert atmosphere of argon using standard Schlenk techniques or in a MBRAUN LABmaster glovebox equipped with a –35 °C freezer. Reaction solvents including tetrahydrofuran (THF), diethyl ether (Et_2O), toluene, and hexanes were purified by distillation over sodium (Na) metal. CH_2Cl_2 (DCM) were purified via distillation over calcium hydride (CaH_2). Deuterated solvents (THF-d_8 and CD_2Cl_2) were purchased from Cambridge Isotope Laboratories. All reaction glassware was oven-dried overnight at 190 ˚C. The NMR spectra were collected on Bruker Avance Neo 500 mHz spectrometers. Proton and carbon signals are reported in ppm and referenced to residual solvent peaks in the deuterated solvent (^{1}H: C_6D_6 δ 7.16, CD_2Cl_2 δ 5.34; ^{13}C: C_6D_6 δ 128.1, CD_2Cl_2 δ 53.8). All solution boron signals are reported in ppm and referenced to $BF_3 \cdot Et_2O$ (^{11}B: $\delta = 0.0$) following the standards and procedures established by IUPAC using the unified scale approach.[1] In some cases, the borosilicate probe from the spectrometer can be observed from –20 to 40 ppm when the signal from the compound is too weak and broad to fully suppress the background signal due to similar frequencies. UV-vis data were collected on a Cary 60 UV-vis spectrometer. Fluorescence data were collected on an Edinburgh Instruments FS5 spectrofluorometer equipped with a double monochromator for excitation and emission. Absolute fluorescence quantum yields were determined using an Edinburgh Instruments FS5 spectrofluorometer equipped with integrating sphere. Samples were prepared in 1 cm square quartz cuvettes with Teflon screw caps. Solutions were prepared in CH_2Cl_2 and the emission data were collected with absorbance values below 0.1 at the excitation wavelength. Fluorescence lifetimes were recorded using a time-correlated single photon counting (TCSPC) method using an Edinburgh Instruments FS5 spectrofluorometer equipped with a double monochromator for excitation and emission. Measurements were made in the right-angle geometry mode, and the emission was collected through a polarizer set to the magic angle. The excitation source was a 337.5 nm excitation LED lamp. The quality of all decay fits was judged to be satisfactory, based on the calculated values of the reduced χ^2 (0.8–1.2) and Durbin Watson parameters and visual inspection of the weighted residuals. Cyclic voltammetry (CV) was performed using a Pine Instruments WaveNow Wireless potentiostat and the Aftermath software package. The Pt coil counter electrode and Ag wire used to construct the reference electrode were obtained from BASi Research Products, and the 3.0 mm glassy carbon disc working electrode was obtained from Pine Instruments. To construct the reference electrode, a glass tube fitted with a Coralpor® frit (BASi Research Products) using heat-shrink tubing (BASi Research Products) and soaked in 0.2 M n-Bu_4NPF_6 in THF overnight. Before running CV, the glass tube was filled with a separate solution containing 0.2 M n-Bu_4NPF_6 and 10 mM $AgNO_3$ in THF before attaching to the silver wire. All CV experiments were performed in an Ar-filled glovebox in an undivided cell sealed by a cap with ports for all electrodes. Cell resistance was determined using cyclic step chronoamperometry, and subsequent CV experiments applied 80% of this resistance value. Ferrocene was added at the end of the experiment, allowing CV data to be referenced to Fc/Fc^+. Compounds **1** and **5** were prepared according to literature procedures.[2] Other compounds were purchased from Sigma Aldrich and used as received.

2. Synthesis and Characterization

Scheme S1. Synthesis of **2**.

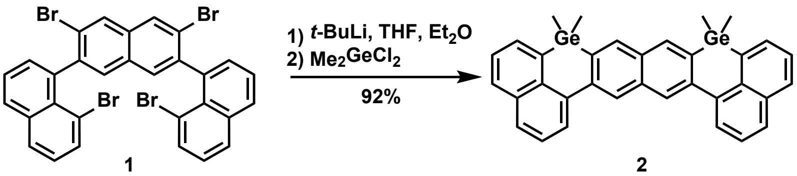

A 100 mL Schlenk flask was charged with **1** (100 mg, 0.144 mmol). The flask was evacuated and refilled with argon three times. Dry THF (5 mL) and dry Et_2O (5 mL) were added, and the solution was cooled to –78 °C. To the stirred mixture, *t*-BuLi (1.7 M in pentane, 0.676 mL, 1.15 mmol, 8 equiv) was added in a dropwise manner. After stirring for 30 min at the same temperature, Me_2GeCl_2 (0.041 mL, 2.5 equiv) was slowly added. The reaction mixture was allowed to warm gradually to room temperature and stirred for 24 h. The crude mixture was purified by flash column chromatography on SiO_2 (hexanes/CH_2Cl_2 = 9:1) to afford **2** as a colorless solid (77.0 mg, 0.132 mmol, 92%).

^{1}H NMR (500 MHz, CD_2Cl_2) δ 8.61 (s, 2H), 8.47 (d, *J* = 7.8 Hz, 2H), 8.18 (s, 2H), 7.95–7.89 (m, 4H), 7.80 (d, *J* = 6.6 Hz, 2H), 7.65 (t, *J* = 7.8 Hz, 2H), 7.55 (dd, *J* = 8.1, 6.6 Hz, 2H), 0.67 (s, 12H) ppm.

^{13}C NMR (126 MHz, CD_2Cl_2) δ 140.4, 136.9, 135.7, 135.6, 134.7, 134.1, 133.4, 133.1, 130.9, 130.2, 130.2, 127.6, 126.5, 126.4 , 125.6, 53.8, –0.7 ppm.

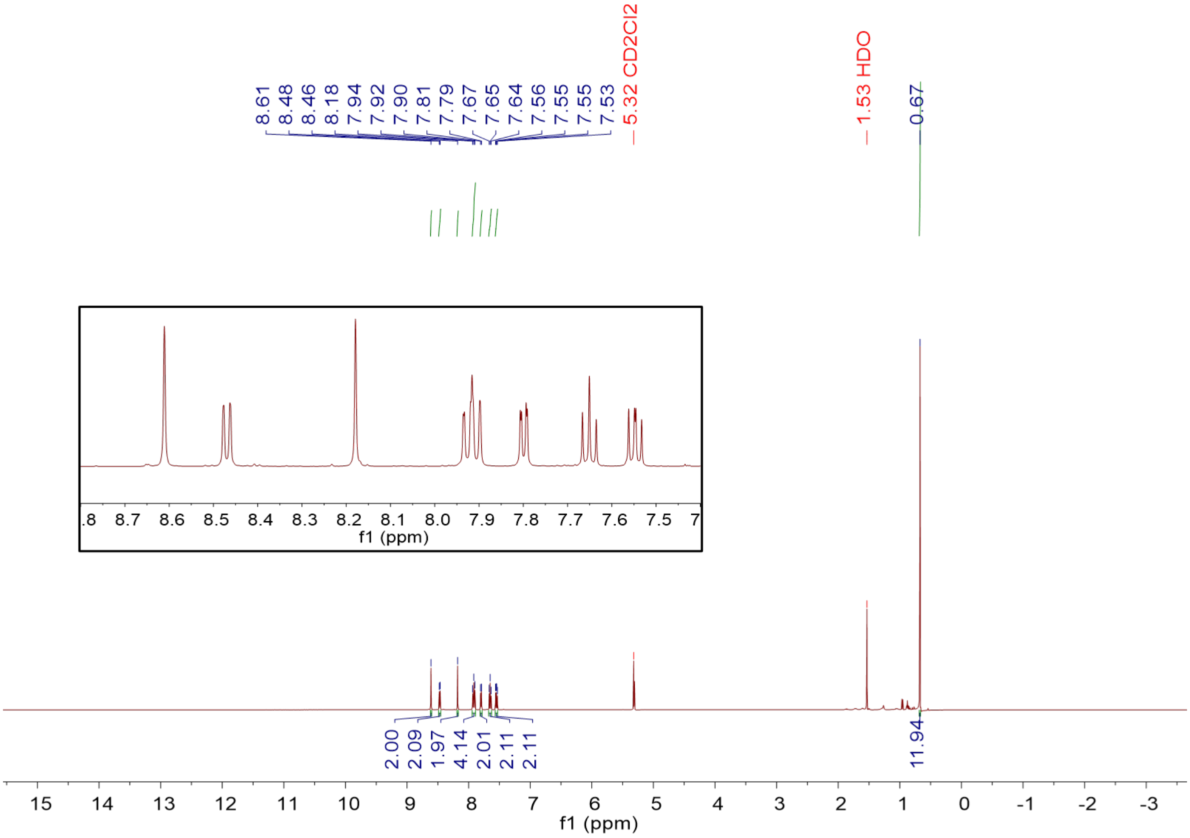

Figure S1. ^{1}H NMR (500 MHz) spectrum of **2** in CD_2Cl_2 (T = 298 K).

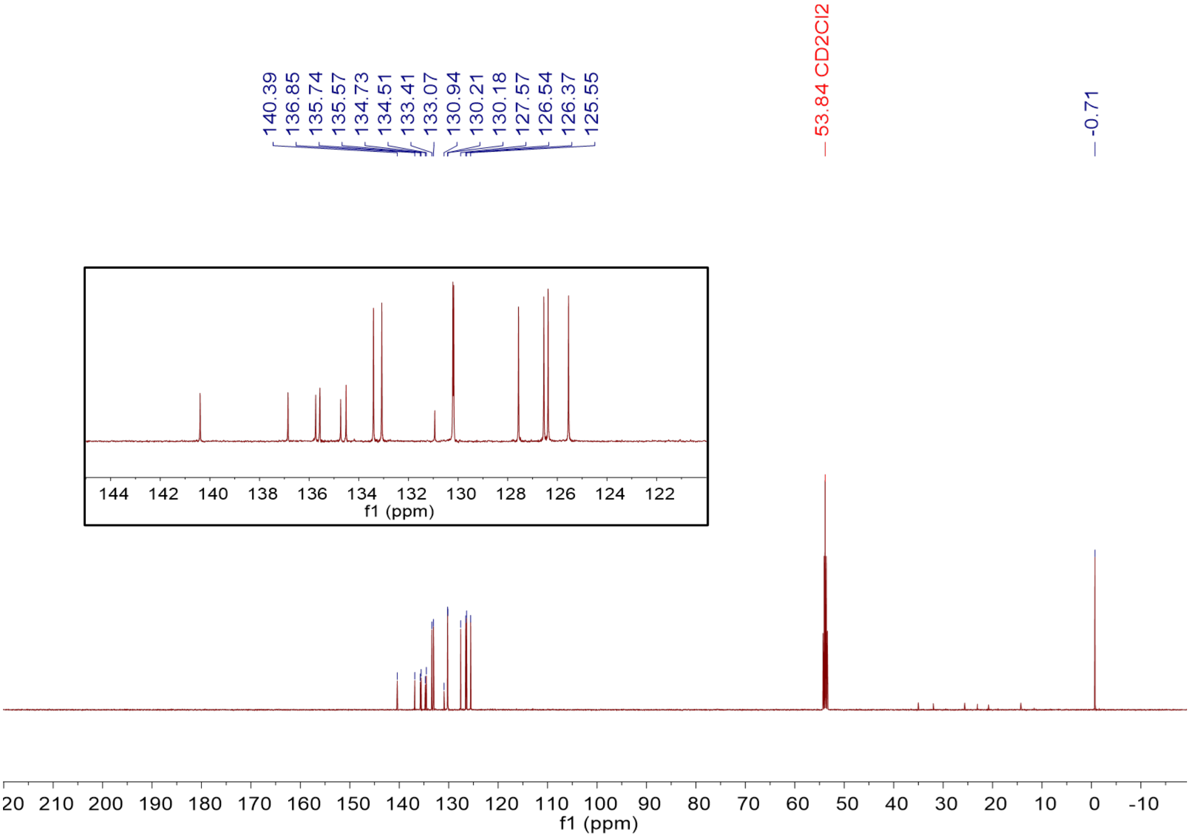

Figure S2. ^{13}C NMR (126 MHz) spectrum of **2** in CD_2Cl_2 (T = 298 K).

Scheme S2. Synthesis of **4**.

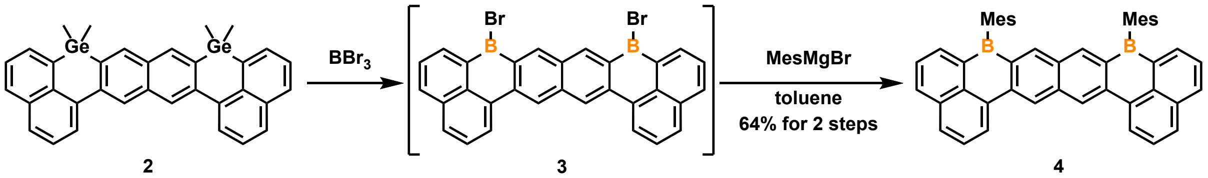

In an anaerobic glovebox, a vial was charged with **2** (50.0 mg, 0.0859 mmol), and neat BBr_3 (0.3 mL) was added in one portion to afford a deep red mixture. The reaction mixture was stirred at room temperature for 24 h, diluted with dry hexanes (10 mL), and the resulting red precipitate was collected by filtration to afford **3** (45.0 mg). Due to its low solubility and high air- and moisture-sensitivity, this material was used directly in the next step without further purification.

In an anaerobic glovebox, a 100 mL Schlenk flask was charged with **3** (45.0 mg) and dry toluene (5 mL). The flask was sealed, removed from the glovebox, and connected to a Schlenk line. The solution was cooled to –78 °C, and MesMgBr (1.0 M in THF, 0.16 mL, 0.16 mmol) was added dropwise. The reaction mixture was allowed to warm gradually to room temperature and stirred for 24 h. The crude product was purified by flash column chromatography on SiO_2 (hexanes/CH_2Cl_2 = 9:1 → 0:10) to afford **4** as a orange crystalline solid (35.0 mg, 0.0550 mmol, 64% over two steps).

^{1}H NMR (500 MHz, THF-*d*$_8$) δ 9.41 (s, 2H), 9.11 (d, J = 7.9 Hz, 2H), 8.47 (s, 2H), 8.32 (d, J = 7.9 Hz, 2H), 8.14 (d, J = 7.9 Hz, 2H), 8.05 (d, J = 6.8 Hz, 2H), 7.86 (t, J = 7.9 Hz, 2H), 7.65 (dd, J = 7.9, 6.8 Hz , 2H), 6.92 (s, 4H), 2.38 (s, 6H), 1.98 (s, 12H) ppm.

^{13}C NMR (126 MHz, THF-*d*$_8$) δ 143.2, 141.7, 140.4, 140.0, 139.1, 137.3, 136.8, 136.0, 135.4, 134.5, 133.8, 133.3, 131.7, 131.0, 127.7, 126.9, 126.8, 126.0, 124.1, 67.2, 25.1, 23.2, 21.3 ppm.

^{11}B NMR (160 MHz, THF-*d*$_8$) δ 66.8 ppm.

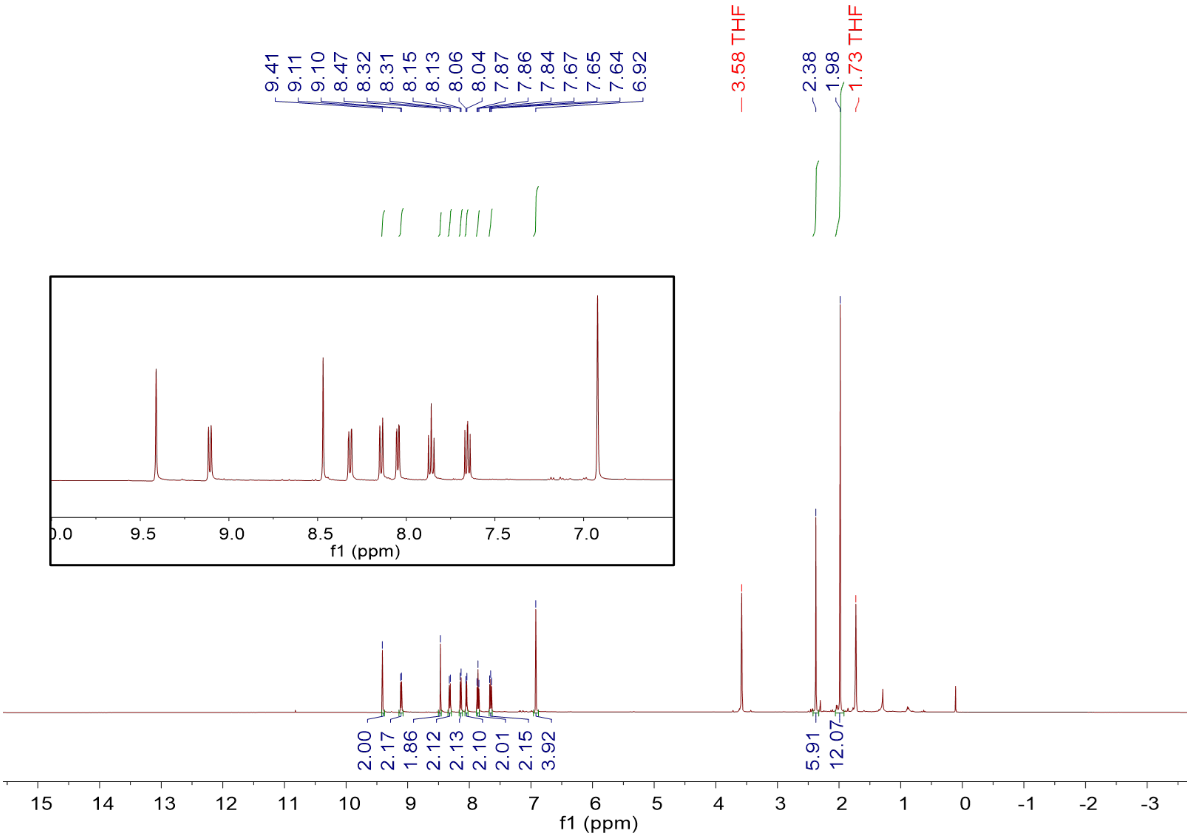

Figure S3. ^{1}H NMR (500 MHz) spectrum of **4** in THF-d_8 (T = 298 K).

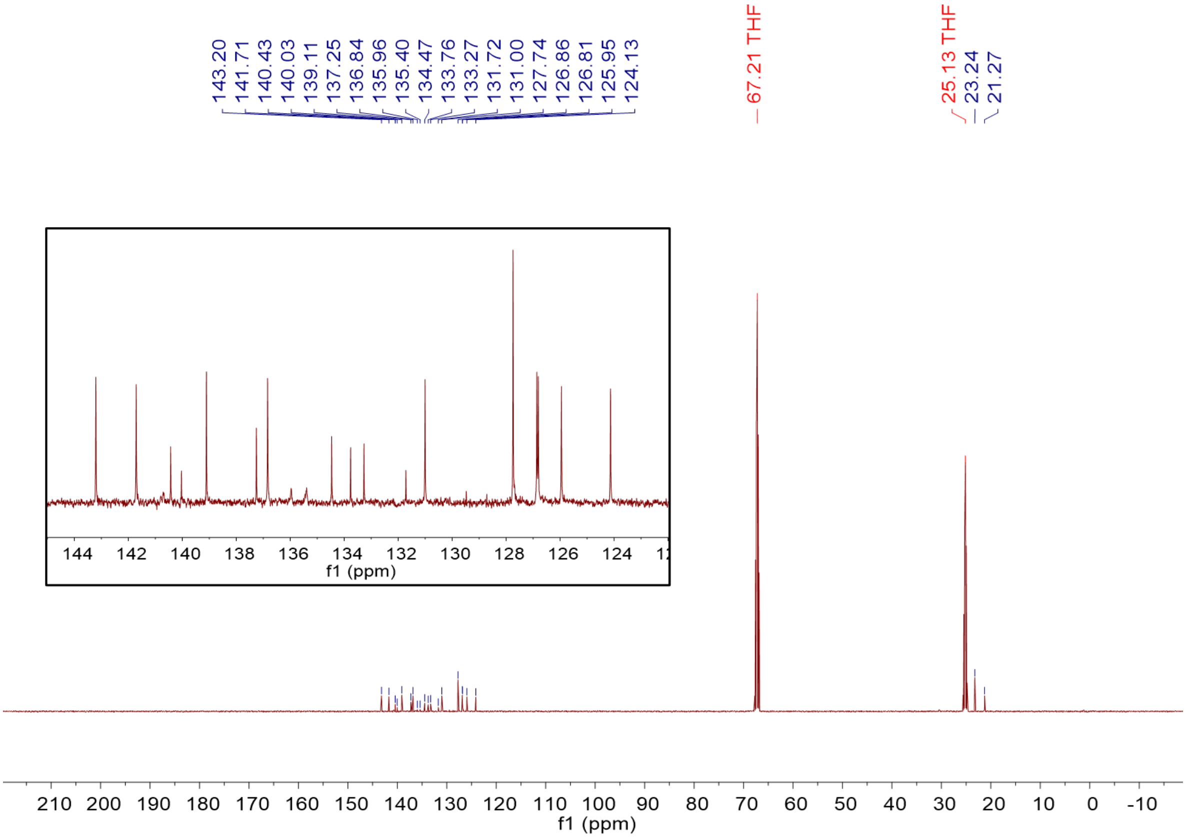

Figure S4. ^{13}C NMR (126 MHz) spectrum of **4** in THF-d_8 (T = 298 K).

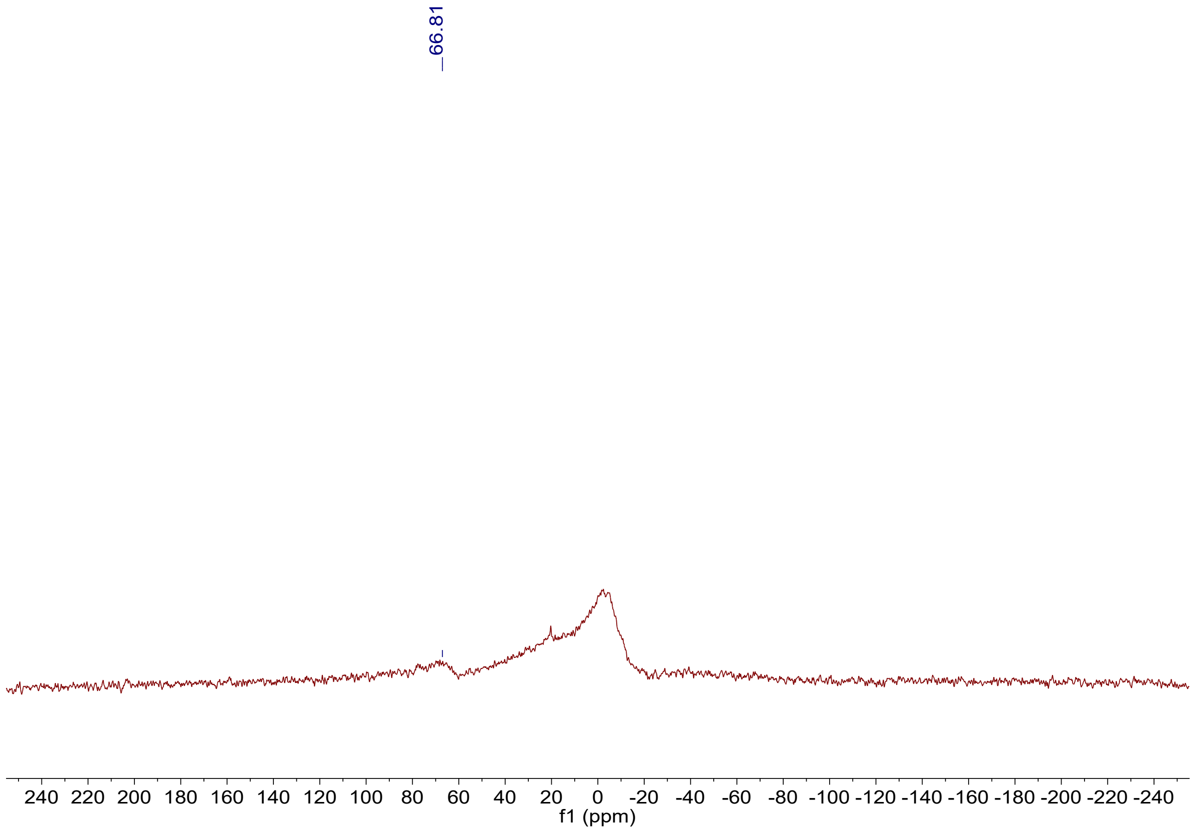

Figure S5. ^{11}B NMR (160 MHz) spectrum of **4** in THF-d_8 (T = 298 K). The ^{11}B NMR resonance of **4** could not be fully resolved due to (i) quadrupolar broadening of the ^{11}B nucleus, (ii) the large molecular size and tricoordinate geometry at the boron center, which further exacerbate quadrupolar broadening, and (iii) the poor solubility of this compound.

Scheme S3. Synthesis of **6**.

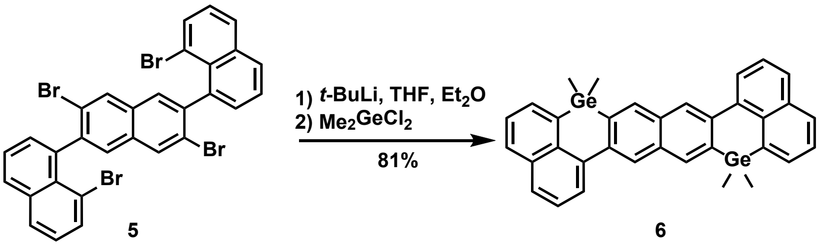

5 **6**

A 100 mL Schlenk flask was charged with **5** (91.0 mg, 0.131 mmol). The flask was evacuated and refilled with argon three times. Dry THF (6 mL) and dry Et_2O (3 mL) were added, and the solution was cooled to –78 °C. To the stirred mixture, *t*-BuLi (1.7 M in pentane, 0.620 mL, 1.05 mmol, 8 equiv) was added in a dropwise manner. After stirring for 30 min at the same temperature, Me_2GeCl_2 (0.038 mL, 2.5 equiv) was slowly added. The reaction mixture was allowed to warm gradually to room temperature and stirred for 24 h. The crude mixture was purified by flash column chromatography on SiO_2 (hexanes/CH_2Cl_2 = 9:1) to afford **2** as a beige solid (62.0 mg, 0.107 mmol, 81%).

^{1}H NMR (400 MHz, CD_2Cl_2) δ 8.56 (s, 2H), 8.47 (d, *J* = 7.6 Hz, 2H), 8.25 (s, 2H), 7.96-7.89 (m, 4H), 7.81 (d, *J* = 6.8 Hz, 2H), 7.66 (t, *J* = 7.8 Hz, 2H), 7.56 (dd, *J* = 7.8, 6.8 Hz , 2H), 0.68 (s, 12H) ppm.

^{13}C NMR (101 MHz, CD_2Cl_2) δ 140.4, 136.7, 135.8, 135.6, 135.1, 134.7, 134.5, 133.3, 133.1, 130.2, 130.2, 126.5, 126.4, 125.8, 125.6, 53.8, –0.7 ppm.

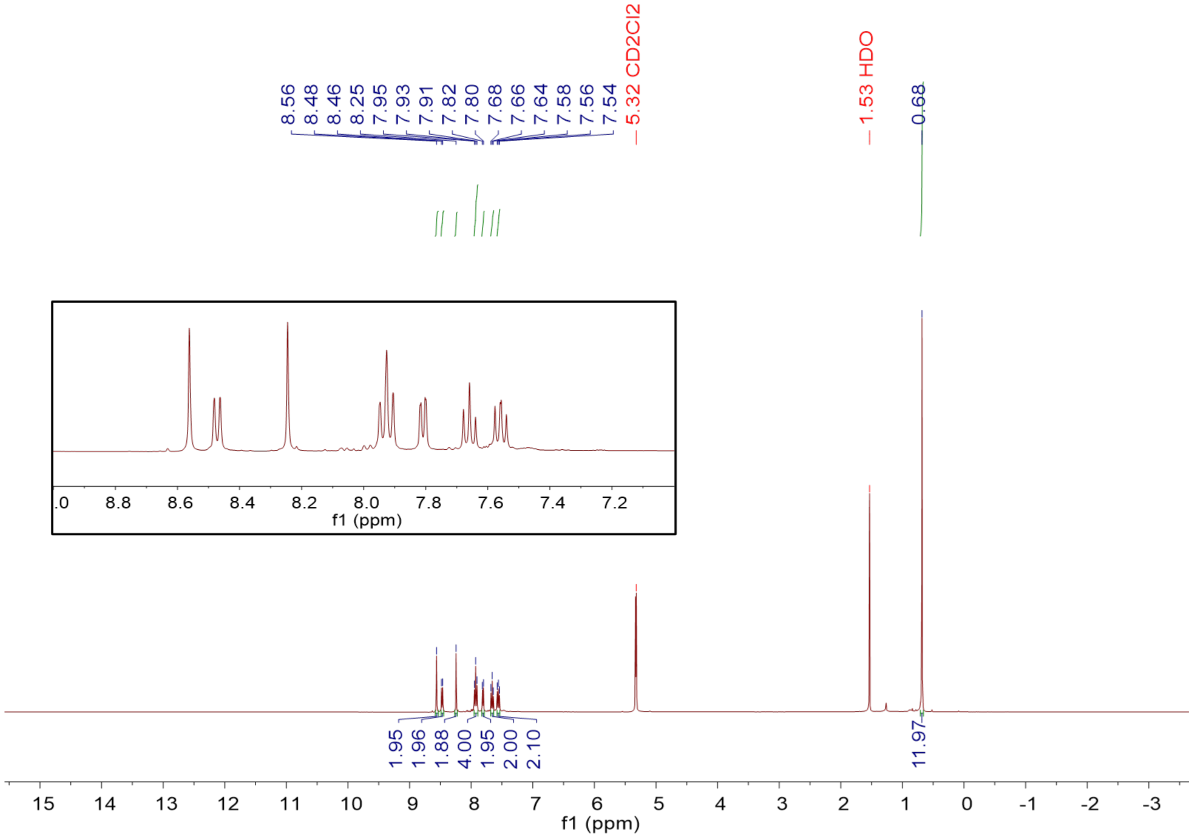

Figure S6. ^{1}H NMR (400 MHz) spectrum of **6** in CD_2Cl_2 ($T = 298$ K).

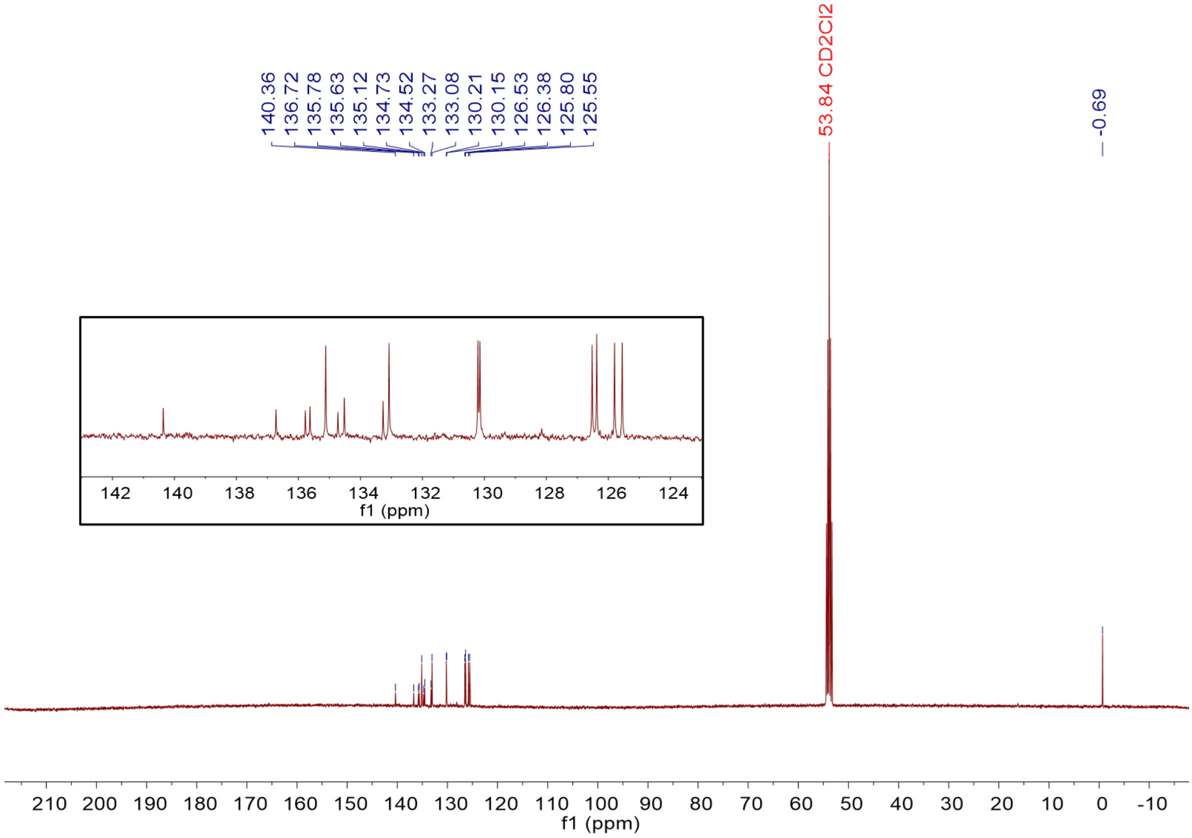

Figure S7. ^{13}C NMR (101 MHz) spectrum of **6** in CD_2Cl_2 ($T = 298$ K).

Scheme S4. Synthesis of **8**.

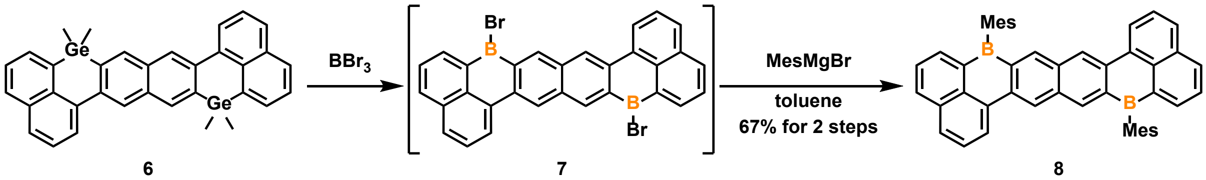

In an anaerobic glovebox, a vial was charged with **6** (62.0 mg, 0.107 mmol), and neat BBr_3 (0.3 mL) was added in one portion to afford a deep red mixture. The reaction mixture was stirred at room temperature for 24 h, diluted with dry hexanes (10 mL), and the resulting red precipitate was collected by filtration to afford **7** (59.0 mg). Due to its low solubility and high air- and moisture-sensitivity, this material was used directly in the next step without further purification.

In an anaerobic glovebox, a 100 mL Schlenk flask was charged with **7** (50.0 mg) and dry toluene (5 mL). The flask was sealed, removed from the glovebox, and connected to a Schlenk line. The solution was cooled to –78 °C, and MesMgBr (1.0 M in THF, 0.23 mL, 0.23 mmol) was added dropwise. The reaction mixture was allowed to warm gradually to room temperature and stirred for 24 h. The crude product was purified by flash column chromatography on SiO_2 (hexanes/CH_2Cl_2 = 9:1 → 0:10) to afford **8** as a red crystalline solid (33.5 mg, 0.0526 mmol, 67% over two steps).

^{1}H NMR (500 MHz, THF-*d*$_8$) δ 9.28 (s, 2H), 9.07 (d, *J* = 7.8 Hz, 2H), 8.68 (s, 2H), 8.31 (d, *J* = 7.8 Hz, 2H), 8.11 (d, *J* = 6.8 Hz, 2H), 8.08 (d, *J* = 7.8 Hz, 2H), 7.77 (t, *J* = 7.8 Hz, 2H), 7.66 (dd, *J* = 7.8, 6.9 Hz, 2H), 7.02 (s, 4H), 2.46 (s, 6H), 2.05 (s, 12H) ppm.

^{13}C NMR (126 MHz, THF-*d*$_8$) δ 142.2, 141.8, 141.0, 139.3, 138.3, 137.7, 137.3, 137.1, 135.7, 135.4, 134.4, 133.6, 133.4, 130.5, 127.8, 126.9, 126.7, 126.0, 125.2, 67.2, 25.1, 23.3, 21.3 ppm.

^{11}B NMR (160 MHz, THF-*d*$_8$) δ 67.5 ppm.

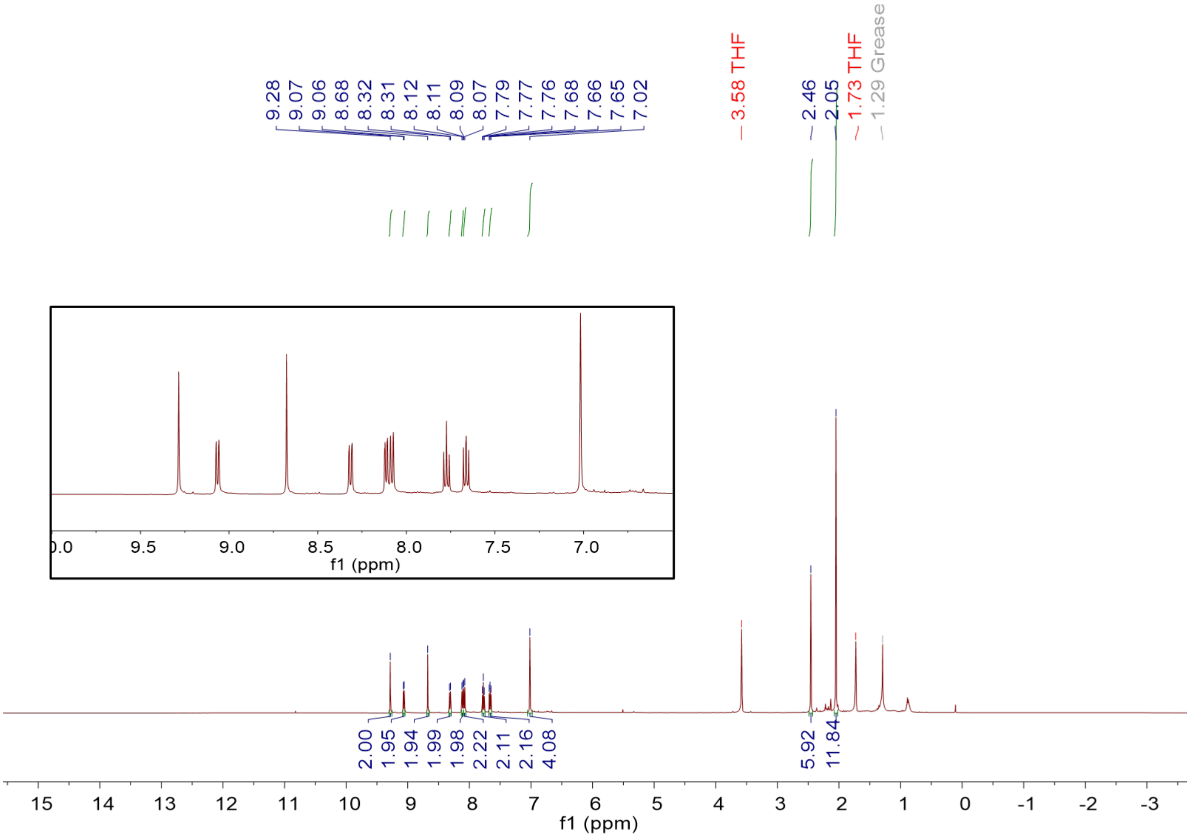

Figure S8. ^{1}H NMR (500 MHz) spectrum of **8** in THF-d_8 (T = 298 K).

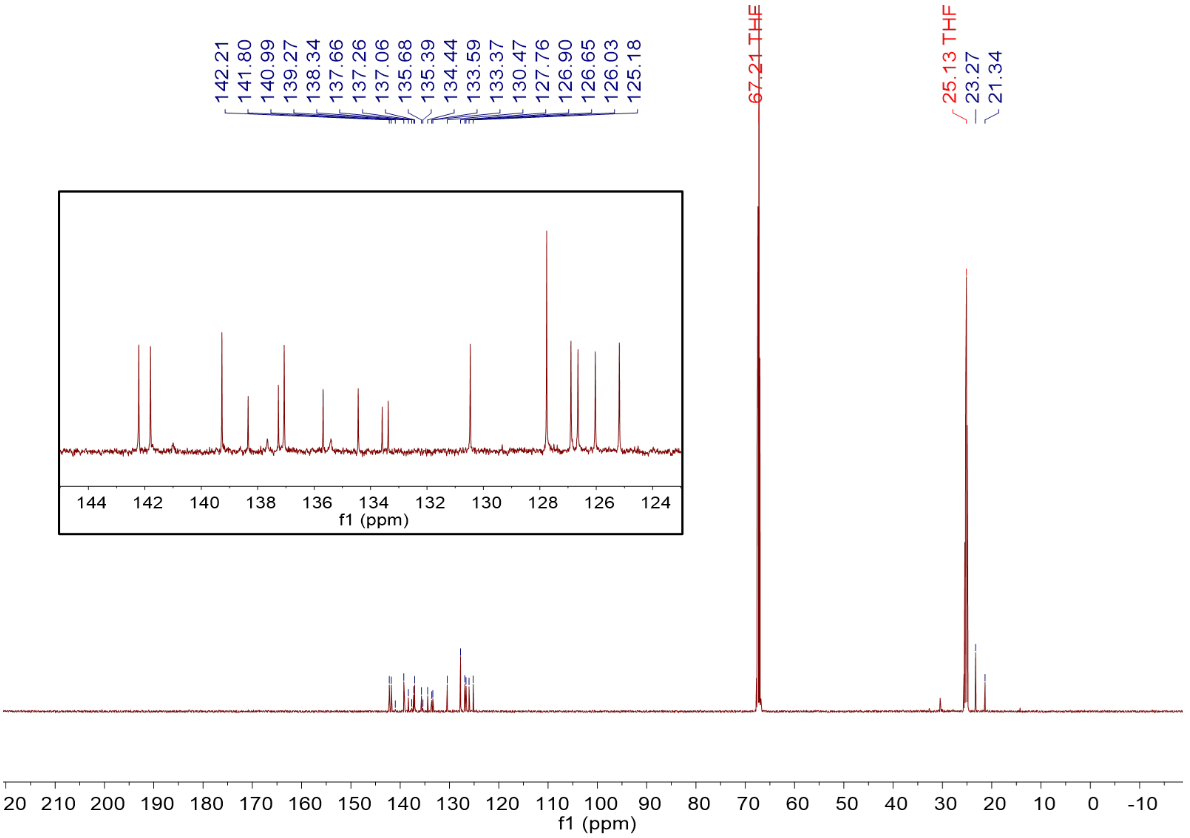

Figure S9. ^{13}C NMR (126 MHz) spectrum of **8** in THF-d_8 (T = 298 K).

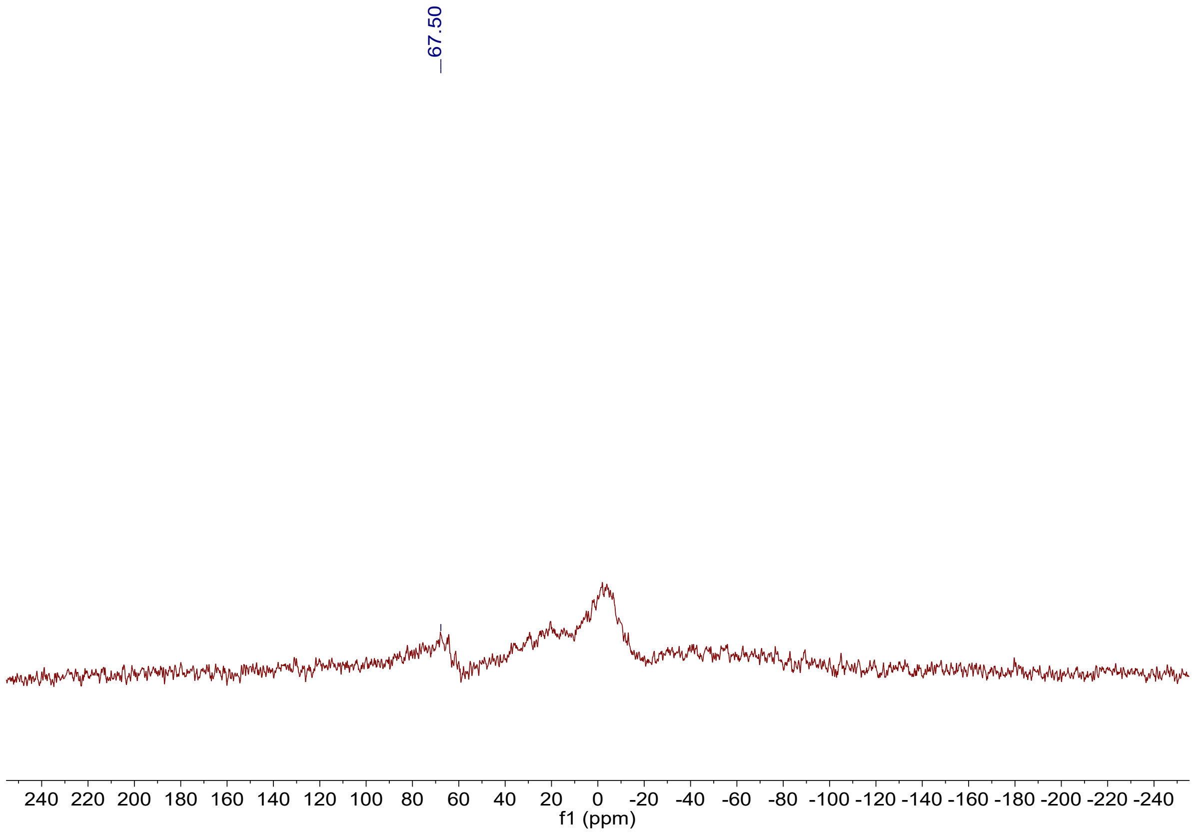

Figure S10. ^{11}B NMR (160 MHz) spectrum of **8** in THF-d_8 (T = 298 K). The ^{11}B NMR resonance of **8** could not be fully resolved due to (i) quadrupolar broadening of the ^{11}B nucleus, (ii) the large molecular size and tricoordinate geometry at the boron center, which further exacerbate quadrupolar broadening, and (iii) the poor solubility of this compound.

Scheme S5. Attempted synthesis of **3** from previously reported disilacycle.[3]

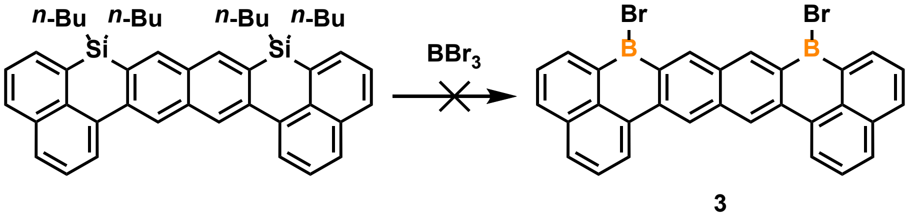

Scheme S6. Attempted synthesis of the distannacycle.

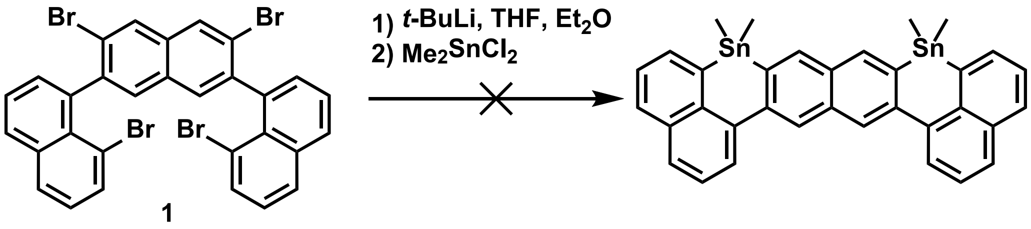

3. Single-crystal X-ray crystallography

Low temperature single crystal X-ray diffraction data were collected on a Bruker D8 Venture PhotonIII Kappa four-circle diffractometer system equipped with dual Incoatec IμS 3.0 micro-focus sealed X-ray tubes (Cu Kα, λ = 1.54178 Å; Mo Kα, λ = 0.71073 Å) and HELIOS double bounce multilayer mirror monochromators. Data reduction was carried out with the program SAINT and semi-empirical absorption correction based on equivalents was performed with the program SADABS.[4] All structures were solved by dual-space methods using SHELXT[5] and refined against F^2 on all data by full-matrix least squares with SHELXL[6] following established refinement strategies[7] within OLEX2 1.5.[8] Non-hydrogen atoms were refined anisotropically, and hydrogen atoms were placed in geometrically calculated positions. Disordered fragments were modelled with the assistance of the implemented DSR tool.[9] The relative occupancies of each position of the disordered sites were freely refined. Constraints and restraints were used on the anisotropic displacement parameters and bond lengths of most of the disordered atoms. Details about data quality and a summary of the residual values of the refinement are listed in Tables S1–S4.

Table S1. Crystal data and structure refinement for **2**.

CCDC number	2499457
Empirical formula	$C_{34}H_{28}Ge_2$
Formula weight	581.74
Temperature/K	100
Crystal system	tetragonal
Space group	$P4_32_12$
a/Å	9.3674(2)
b/Å	9.3674(2)
c/Å	36.3077(13)
α/°	90
β/°	90
γ/°	90
Volume/Å^3	3185.93(18)
Z	4
ρ_{calc}g/cm^3	1.213
μ/mm^{-1}	1.904
F(000)	1184
Crystal size/mm^3	0.201 × 0.174 × 0.12
Radiation	MoKα (λ = 0.71073)
2Θ range for data collection/°	4.49 to 61.12
Index ranges	$-13 \leq h \leq 13$, $-13 \leq k \leq 13$, $-51 \leq l \leq 51$
Reflections collected	165155
Independent reflections	4876 [R_{int} = 0.0892, R_{sigma} = 0.0220]
Data/restraints/parameters	4876/0/166
Goodness-of-fit on F^2	1.064
Final R indexes [I>=2σ (I)]	R_1 = 0.0393, wR_2 = 0.1035
Final R indexes [all data]	R_1 = 0.0411, wR_2 = 0.1043
Largest diff. peak/hole / e Å^{-3}	0.56/-0.53
Flack parameter	0.080(5)

Table S2. Crystal data and structure refinement for **4**.

CCDC number	2499456
Empirical formula	$C_{48}H_{38}B_2$
Formula weight	636.4
Temperature/K	100
Crystal system	monoclinic
Space group	$P2_1/n$
a/Å	7.5540(9)
b/Å	15.9008(17)
c/Å	28.717(3)
α/°	90
β/°	92.598(4)
γ/°	90
Volume/Å^3	3445.8(7)
Z	4
ρ_{calc}g/cm^3	1.227
μ/mm^{-1}	0.068
F(000)	1344
Crystal size/mm^3	0.235 × 0.225 × 0.019
Radiation	MoKα (λ = 0.71073)
2Θ range for data collection/°	3.824 to 54.354
Index ranges	$-9 \leq h \leq 9$, $-20 \leq k \leq 18$, $-36 \leq l \leq 36$
Reflections collected	161107
Independent reflections	7529 [R_{int} = 0.0831, R_{sigma} = 0.0450]
Data/restraints/parameters	7529/0/457
Goodness-of-fit on F^2	1.097
Final R indexes [I>=2σ (I)]	R_1 = 0.1389, wR_2 = 0.3399
Final R indexes [all data]	R_1 = 0.1596, wR_2 = 0.3499
Largest diff. peak/hole / e Å^{-3}	0.45/-0.47

Table S3. Crystal data and structure refinement for **6**.

CCDC number	2499455
Empirical formula	$C_{34}H_{28}Ge_2$
Formula weight	581.74
Temperature/K	100
Crystal system	monoclinic
Space group	C_2/c
a/Å	24.7535(9)
b/Å	8.3982(4)
c/Å	28.0894(13)
α/°	90
β/°	99.295(2)
γ/°	90
Volume/Å^3	5762.7(4)
Z	8
ρ_{calc}g/cm^3	1.341
μ/mm^{-1}	2.106
F(000)	2368
Crystal size/mm^3	0.151 × 0.11 × 0.09
Radiation	MoKα (λ = 0.71073)
2Θ range for data collection/°	4.788 to 61.114
Index ranges	$-35 \leq h \leq 31$, $-11 \leq k \leq 12$, $-40 \leq l \leq 40$
Reflections collected	118125
Independent reflections	8793 [R_{int} = 0.0542, R_{sigma} = 0.0237]
Data/restraints/parameters	8793/0/329
Goodness-of-fit on F^2	1.034
Final R indexes [I>=2σ (I)]	R_1 = 0.0293, wR_2 = 0.0811
Final R indexes [all data]	R_1 = 0.0352, wR_2 = 0.0841
Largest diff. peak/hole / e Å^{-3}	0.74/-0.53

Table S4. Crystal data and structure refinement for **8**.

CCDC number	2499454
Empirical formula	$C_{48}H_{38}B_2\cdot2(C_7H_8)$
Formula weight	820.67
Temperature/K	100(2)
Crystal system	monoclinic
Space group	$C2/c$
a/Å	28.5047(13)
b/Å	10.3751(5)
c/Å	15.6252(7)
α/°	90
β/°	97.348(3)
γ/°	90
Volume/Å^3	4583.0(4)
Z	4
ρ_{calc}g/cm^3	1.189
μ/mm^{-1}	0.497
F(000)	1744
Crystal size/mm^3	0.192 × 0.058 × 0.057
Radiation	CuKα (λ = 1.54178)
2Θ range for data collection/°	9.08 to 157.778
Index ranges	$-36 \leq h \leq 36$, $-12 \leq k \leq 13$, $-19 \leq l \leq 17$
Reflections collected	34807
Independent reflections	4881 [R_{int} = 0.0331, R_{sigma} = 0.0219]
Data/restraints/parameters	4881/513/357
Goodness-of-fit on F^2	1.037
Final R indexes [I>=2σ (I)]	R_1 = 0.0440, wR_2 = 0.1122
Final R indexes [all data]	R_1 = 0.0542, wR_2 = 0.1224
Largest diff. peak/hole / e Å^{-3}	0.18/-0.24

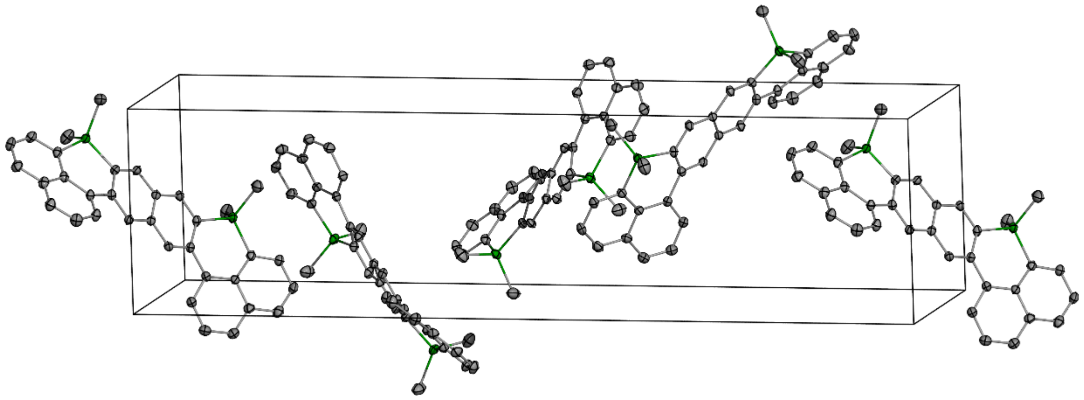

Figure S11. Packing structure of **2** in a unit cell. Thermal ellipsoids were drawn at the 50% probability level; H atoms are omitted for clarity.

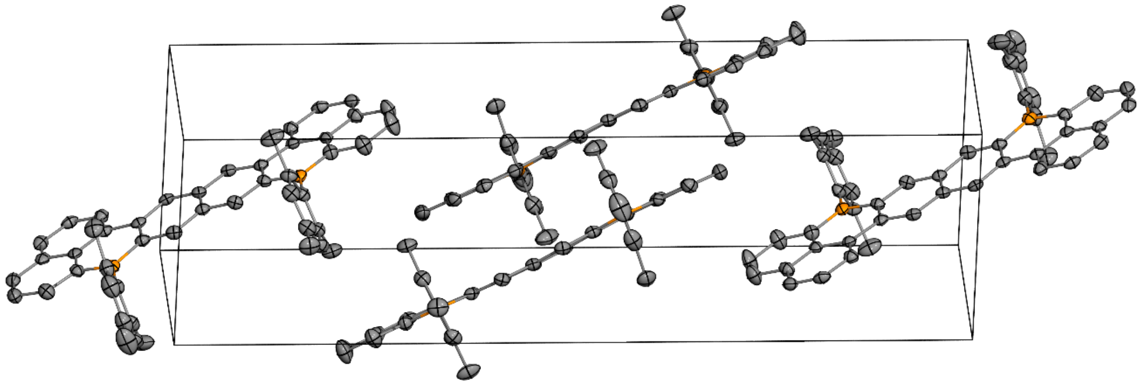

Figure S12. Packing structure of **4** in a unit cell. Thermal ellipsoids were drawn at the 50% probability level; H atoms are omitted for clarity.

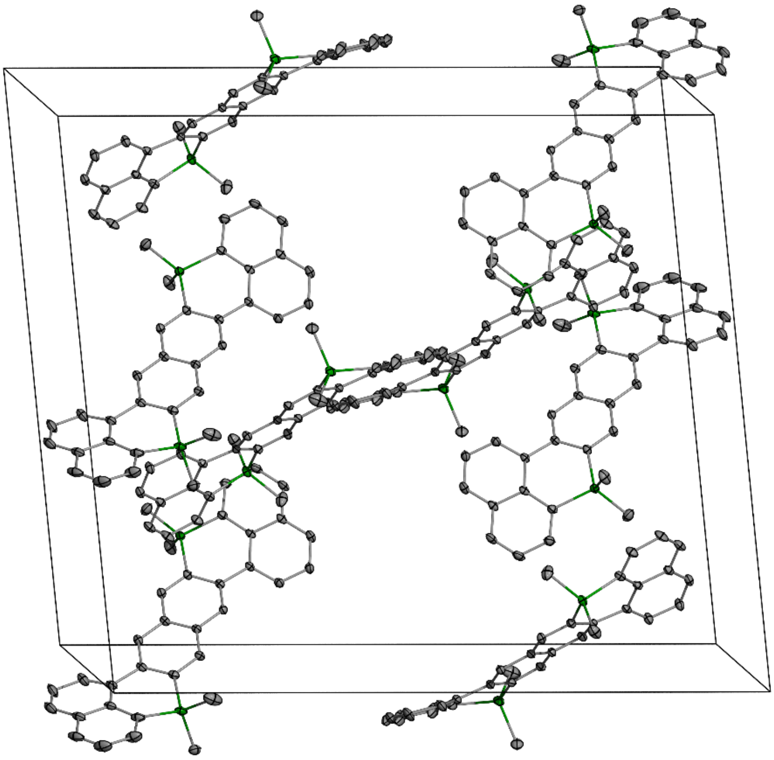

Figure S13. Packing structure of **6** in a unit cell. Thermal ellipsoids were drawn at the 50% probability level; H atoms are omitted for clarity.

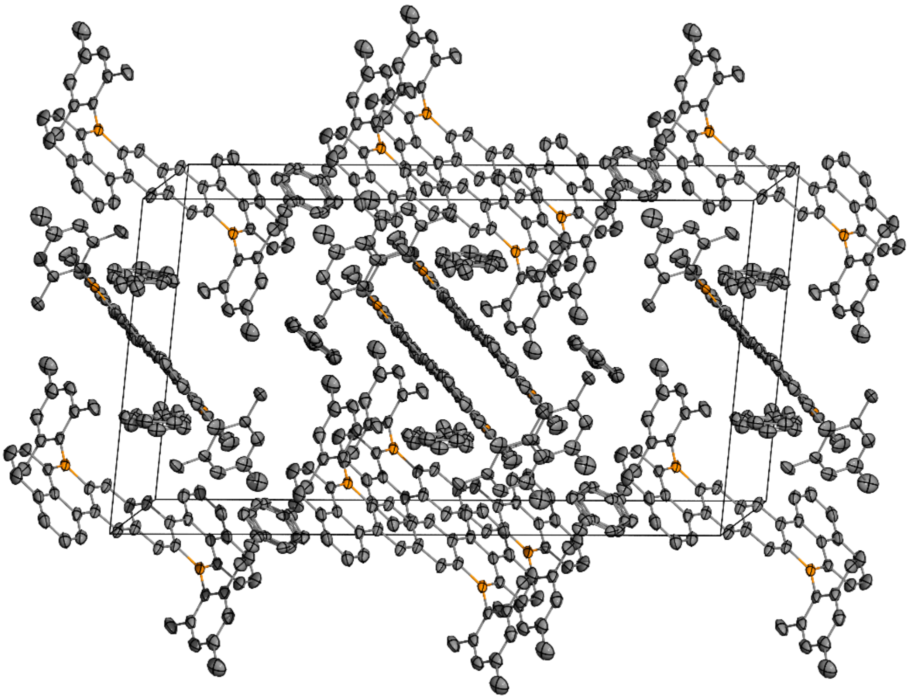

Figure S14. Packing structure of **8** in a unit cell. Thermal ellipsoids were drawn at the 50% probability level; H atoms are omitted for clarity.

4. Photophysical properties

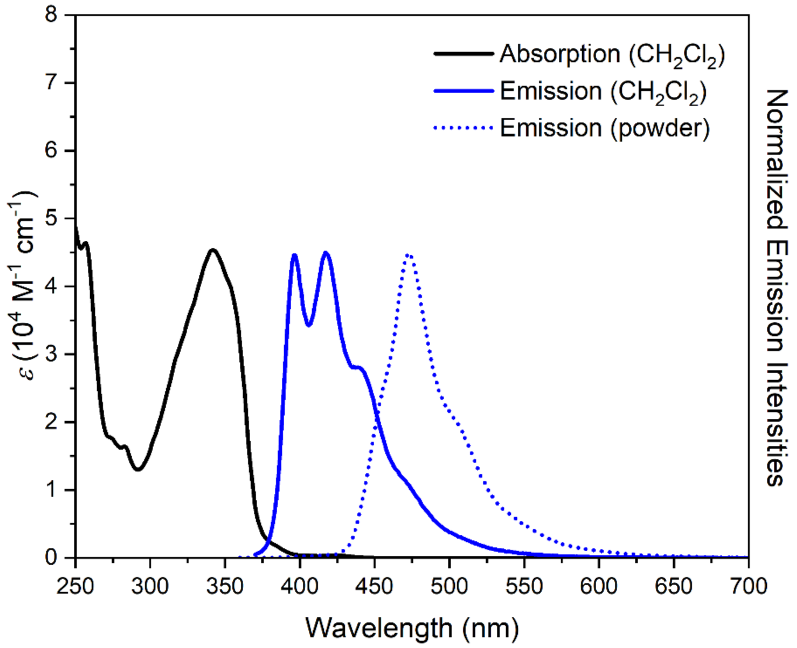

Figure S15. Absorption and emission spectra of **2**.

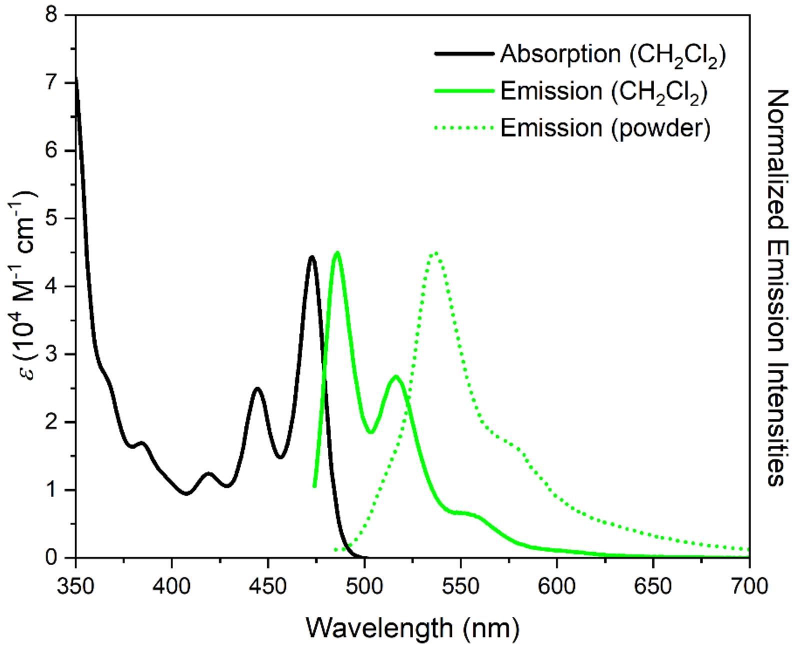

Figure S16. Absorption and emission spectra of **4**.

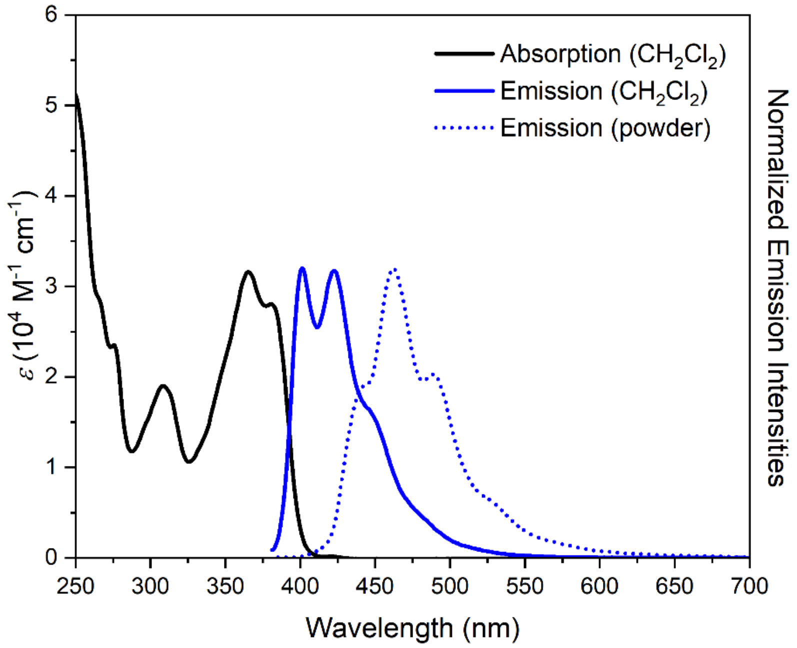

Figure S17. Absorption and emission spectra of **6**.

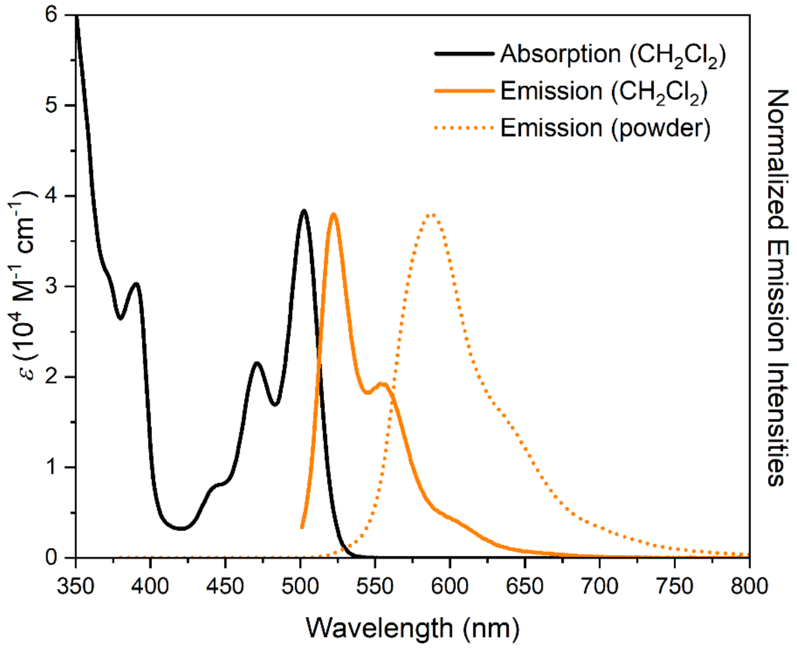

Figure S18. Absorption and emission spectra of **8**.

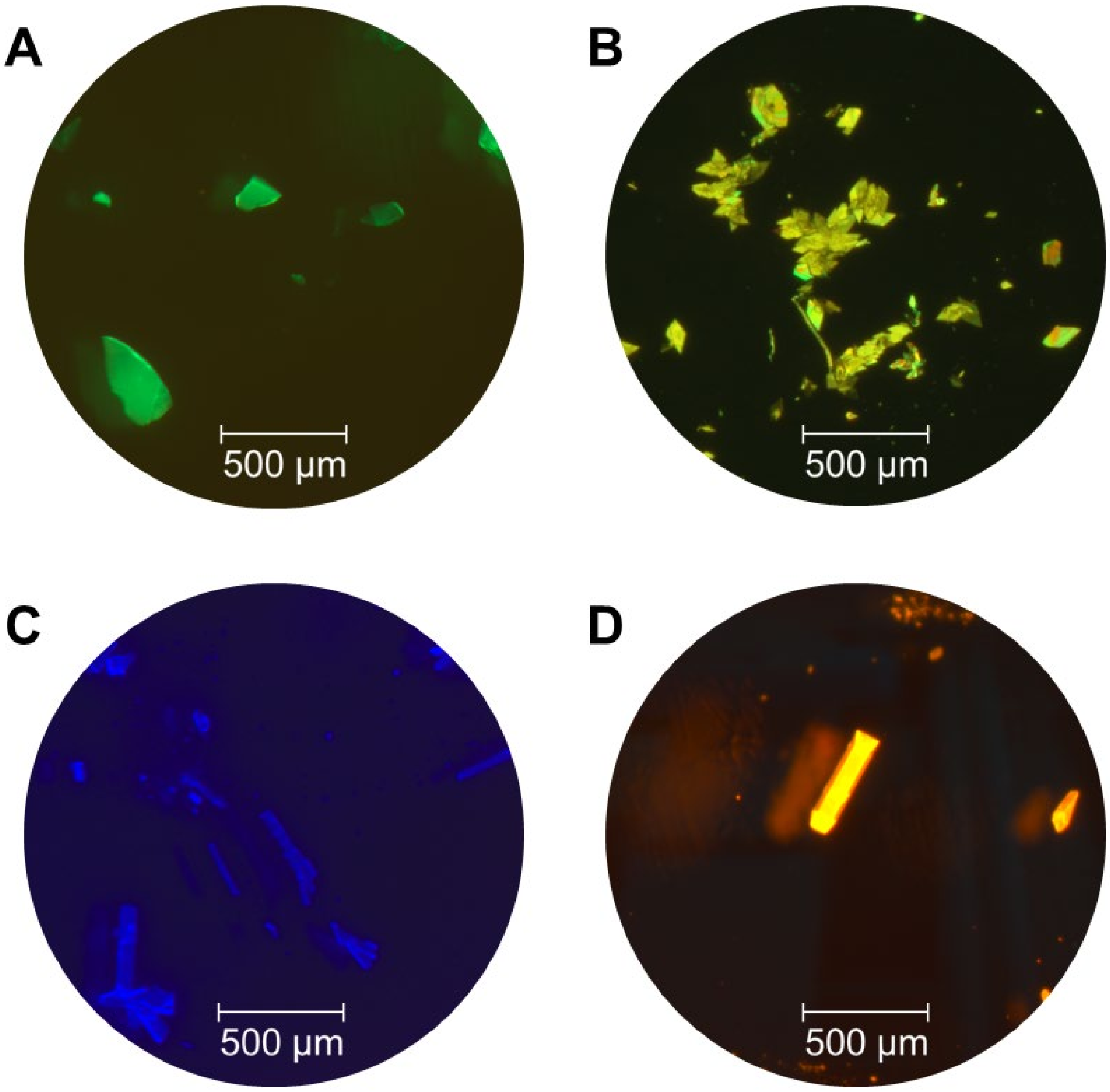

Figure S19. Microscopic images of the crystals of **2** (A), **4** (B), **6** (C), and **8** (D) under UV light irradiation.

5. Electrochemical measurements

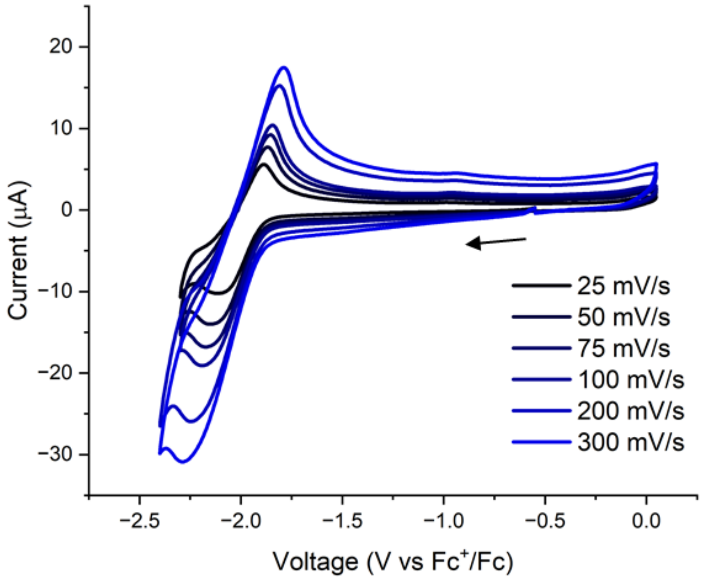

Figure S20. Scan rate dependence of reduction wave in the cyclic voltammogram of **4** on glassy carbon working electrode with *n*-Bu_4NPF_6 (0.1 M) as the supporting electrolyte. Sample concentration = 2 mM.

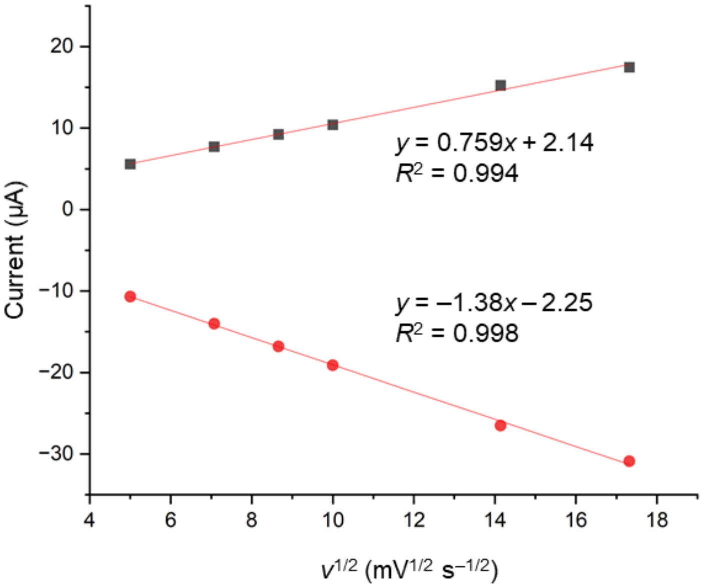

Figure S21. Randles-Sevcik plot of the reduction feature in the cyclic voltammogram of **4**.

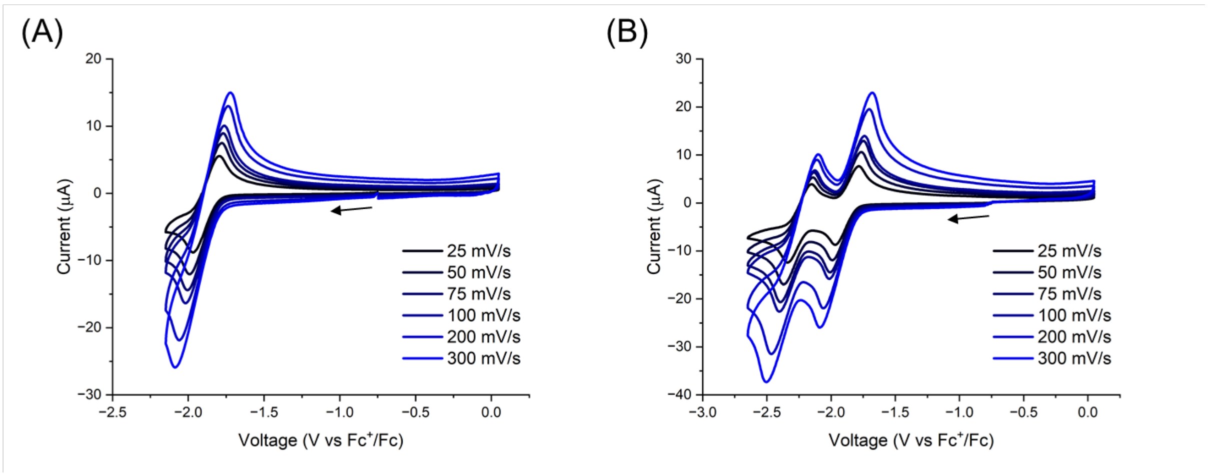

Figure S22. Scan rate dependence of (A) the first and (B) the second reduction waves in the cyclic voltammogram of **8** on glassy carbon working electrode with *n*-Bu$_4$NPF$_6$ (0.1 M) as the supporting electrolyte. Sample concentration = 2 mM.

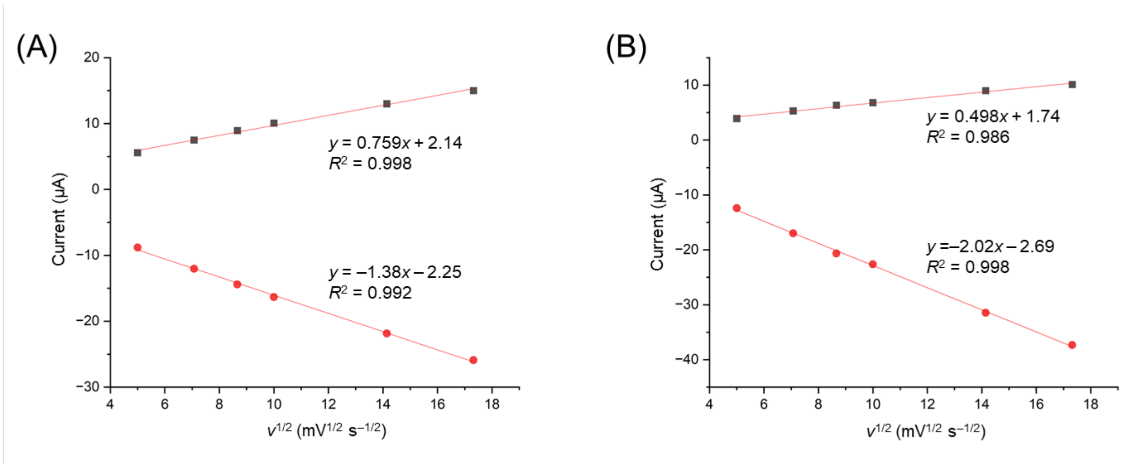

Figure S23. Randles-Sevcik plot of (A) the first and (B) the second reduction features in the cyclic voltammogram of **8**.

6. Theoretical calculations

For compounds **2**, **4**, **6**, and **8**, geometry optimizations were performed at the B3LYP-D3(BJ)/def2-SVP level of theory in Orca 6.0.0.[10-14] Single point calculations were performed at the B3LYP-D3(BJ)/def2-TZVP level of theory using the optimized geometries. Both optimizations and single-point TD-DFT calculations were performed in solvent using the conductor-like polarizable continuum model (CPCM) with parameters for CH_2Cl_2.[15] All optimizations utilized the resolution of identity approximation for both Coulomb and Hartree−Fock exchange integrals and a 590-point integration grid. Harmonic frequency calculations were carried out analytically to confirm that optimized geometries were minima. Vertical excitations were calculated using TD-DFT at the B3LYP-D3(BJ)/def2-TZVP//B3LYP-D3(BJ)/def2-SVP level of theory Orca 6.0.0.[16]

For mechanistic studies depicted in Fig. 2, geometry optimizations were performed at the B3LYP-D3(BJ)/def2-SVP level of theory in Orca 6.0.0 using the CPCM with parameters for BBr_3 ($\varepsilon = 2.58$). All optimizations utilized the resolution of identity approximation for both Coulomb and Hartree−Fock exchange integrals and a 590-point integration grid. Harmonic frequency calculations were carried out analytically to confirm that optimized geometries were minima. All transition-state optimizations utilized the quasi-Newtonian eigenvector following (EF) algorithm implemented in Orca 6.0.0. Energy diagrams created with EveRplot.[17]

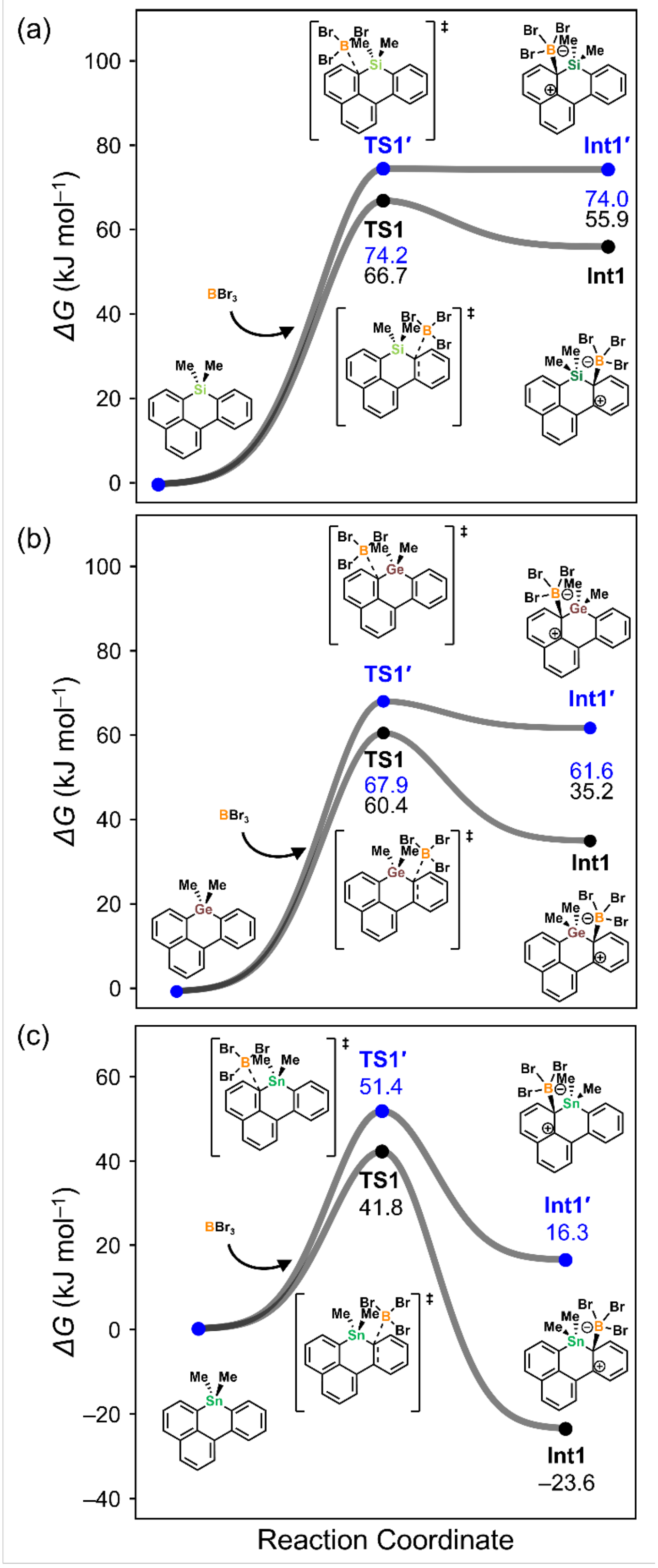

Figure S24. Comparison of the calculated energy profiles of the encounter complexes for (a) silacycle, (b) germacycle, and (c) stannacycle systems. For each system, interaction of BBr_3 with the phenyl ring leads to a more stable encounter complex than interaction with the naphthalene ring.

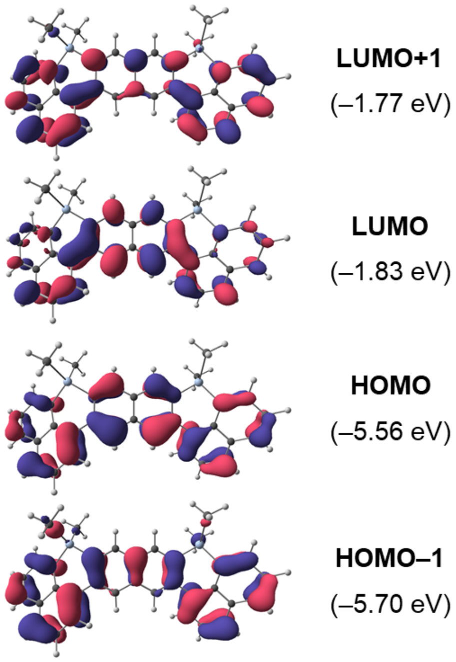

Figure S24. Frontier molecular orbitals (FMOs) of **2**, calculated at the B3LYP-D3(BJ)/def2-TZVP level of theory (isovalue = 0.03).

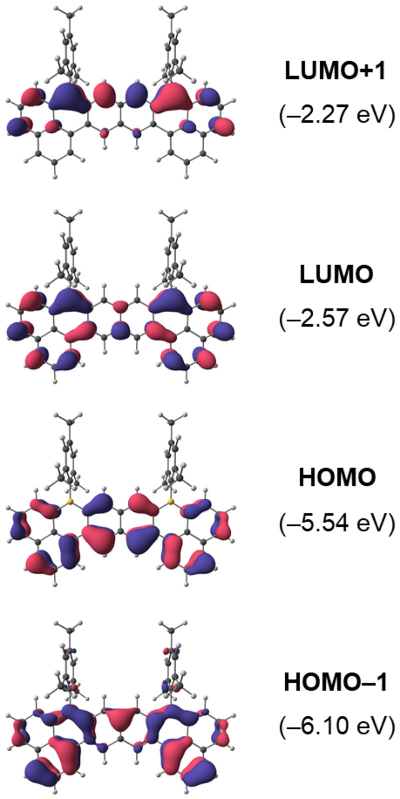

Figure S25. Frontier molecular orbitals (FMOs) of **4**, calculated at the B3LYP-D3(BJ)/def2-TZVP level of theory (isovalue = 0.03).

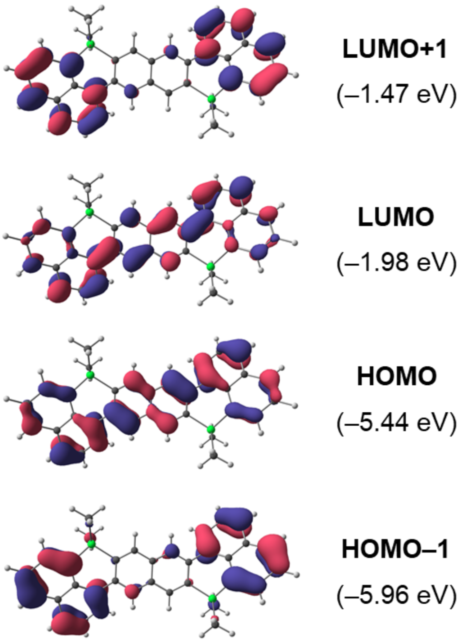

Figure S26. Frontier molecular orbitals (FMOs) of **6**, calculated at the B3LYP-D3(BJ)/def2-TZVP level of theory (isovalue = 0.03).

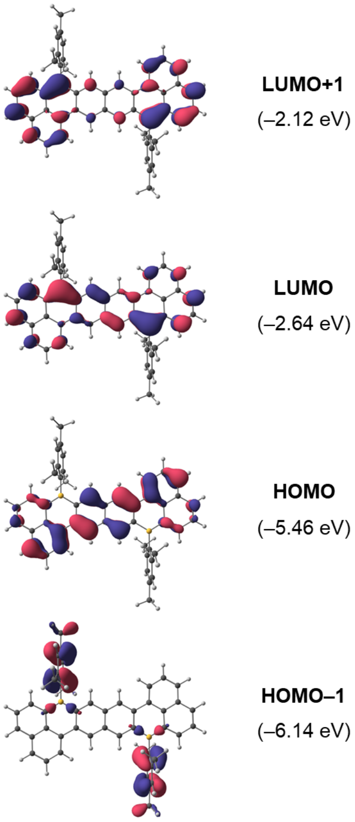

Figure S27. Frontier molecular orbitals (FMOs) of **8**, calculated at the B3LYP-D3(BJ)/def2-TZVP level of theory (isovalue = 0.03).

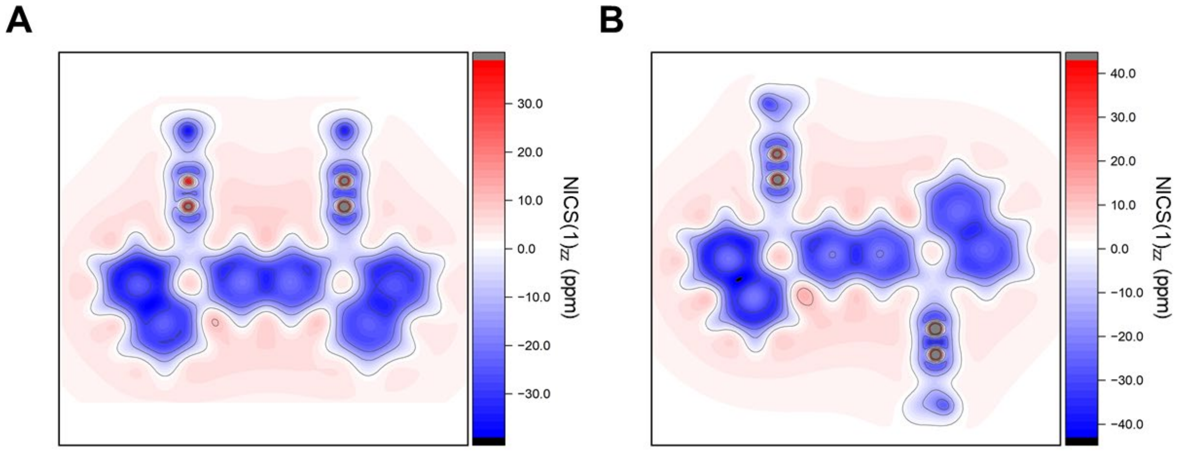

Figure S28. Calculated 2D-NICS(1)$_{zz}$ maps for (A) **4** and (B) **8** at 1 Å above the molecular XY plane. Chemical shifts were evaluated at the B3LYP-D3(BJ)/def2-SVP level of theory.

Table S5. Calculated vertical excitation energies of **2** at the B3LYP-D3(BJ)/def2-TZVP (CPCM, CH_2Cl_2) level of theory.

Excited state	*E* (eV)	*λ* (nm)	*f*	Composition
1	3.261	380.2	0.04774	HOMO–2→LUMO+1 (2%) HOMO–1→LUMO (33%) HOMO–1→LUMO+2 (2%) HOMO→LUMO+1 (60%)
2	3.443	360.2	0.00668	HOMO→LUMO (96%)
3	3.466	357.8	1.39787	HOMO–1→LUMO (62%) HOMO→LUMO+1 (35%)
4	3.624	342.1	0.14831	HOMO–1→LUMO+1 (95%) HOMO→LUMO+2 (2%)
5	3.837	323.1	0.01273	HOMO–2→LUMO (28%) HOMO→LUMO+2 (69%)

Table S6. Calculated vertical excitation energies of **4** at the B3LYP-D3(BJ)/def2-TZVP (CPCM, CH_2Cl_2) level of theory.

Excited state	*E* (eV)	*λ* (nm)	*f*	Composition
1	2.594	478.0	0.86361	HOMO–1→LUMO+1 (2%) HOMO→LUMO (95%)
2	2.847	435.5	0.02092	HOMO–1→LUMO (2%) HOMO→LUMO+1 (95%)
3	2.980	416.1	0.00002	HOMO–3→LUMO+1 (21%) HOMO–2→LUMO (78%)
4	2.989	414.8	0.00001	HOMO–3→LUMO (75%) HOMO–2→LUMO+1 (24%)
5	3.203	387.1	0.18720	HOMO–10→LUMO+1 (1%) HOMO–6→LUMO (3%) HOMO–1→LUMO (90%) HOMO→LUMO+1 (2%)

Table S7. Calculated vertical excitation energies of **6** at the B3LYP-D3(BJ)/def2-TZVP (CPCM, CH_2Cl_2) level of theory.

Excited state	*E* (eV)	*λ* (nm)	*f*	Composition
1	3.129	396.2	1.13709	HOMO→LUMO (97%)
2	3.433	361.2	0.00043	HOMO–2→LUMO (39%) HOMO→LUMO+2 (57%)
3	3.542	350.0	0.000002	HOMO–1→LUMO (48%) HOMO–1→LUMO+2 (2%) HOMO→LUMO+1 (48%)
4	3.697	335.3	0.00299	HOMO–1→LUMO (47%) HOMO→LUMO+1 (47%)
5	3.874	320.0	0.21178	HOMO–2→LUMO (54%) HOMO→LUMO+2 (38%)

Table S8. Calculated vertical excitation energies of **8** at the B3LYP-D3(BJ)/def2-TZVP (CPCM, CH_2Cl_2) level of theory.

Excited state	*E* (eV)	*λ* (nm)	*f*	Composition
1	2.430	510.1	0.56177	HOMO–6→LUMO+2 (2%) HOMO→LUMO (96%)
2	2.906	426.7	0.000004	HOMO–2→LUMO+1 (8%) HOMO–1→LUMO (91%)
3	2.917	425.0	0.00001	HOMO–2→LUMO (90%) HOMO–1→LUMO+1 (8%)
4	2.961	418.7	0.0000004	HOMO–3→LUMO (1%) HOMO→LUMO+1 (95%)
5	3.117	397.8	0.35407	HOMO–6→LUMO (6%) HOMO→LUMO+2 (88%)

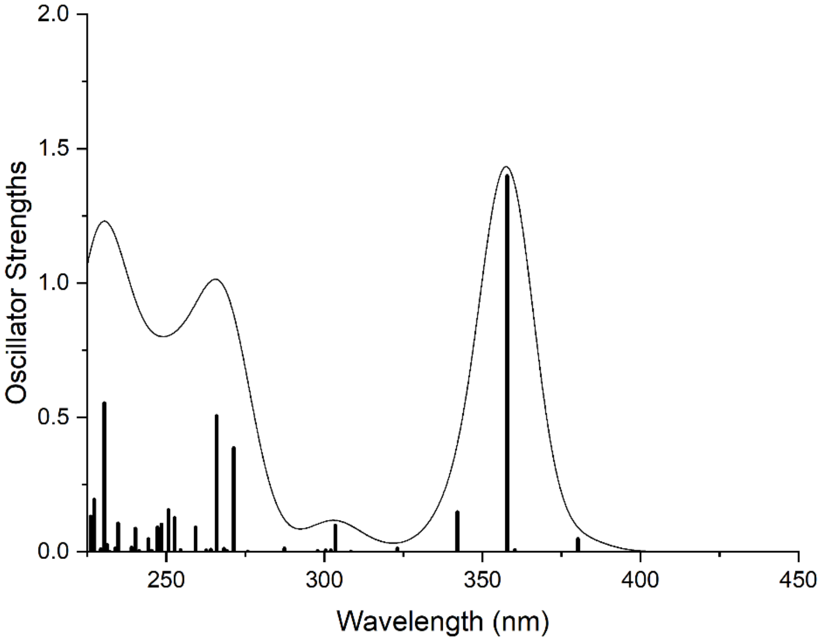

Figure S29. Calculated absorption spectrum of **2** with the oscillator strengths at the B3LYP-D3(BJ)/def2-TZVP (CPCM, CH_2Cl_2) level of theory.

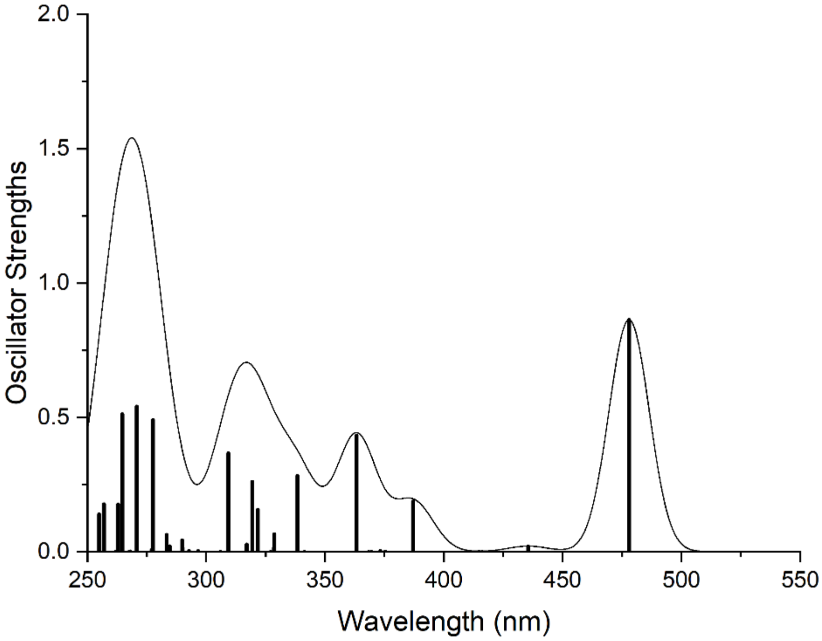

Figure S30. Calculated absorption spectrum of **4** with the oscillator strengths at the B3LYP-D3(BJ)/def2-TZVP (CPCM, CH_2Cl_2) level of theory.

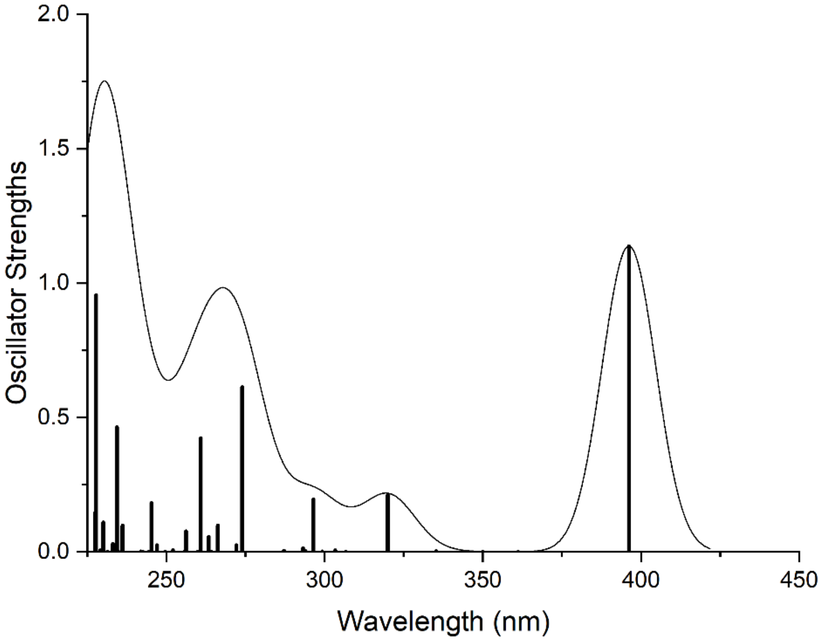

Figure S31. Calculated absorption spectrum of **6** with the oscillator strengths at the B3LYP-D3(BJ)/def2-TZVP (CPCM, CH_2Cl_2) level of theory.

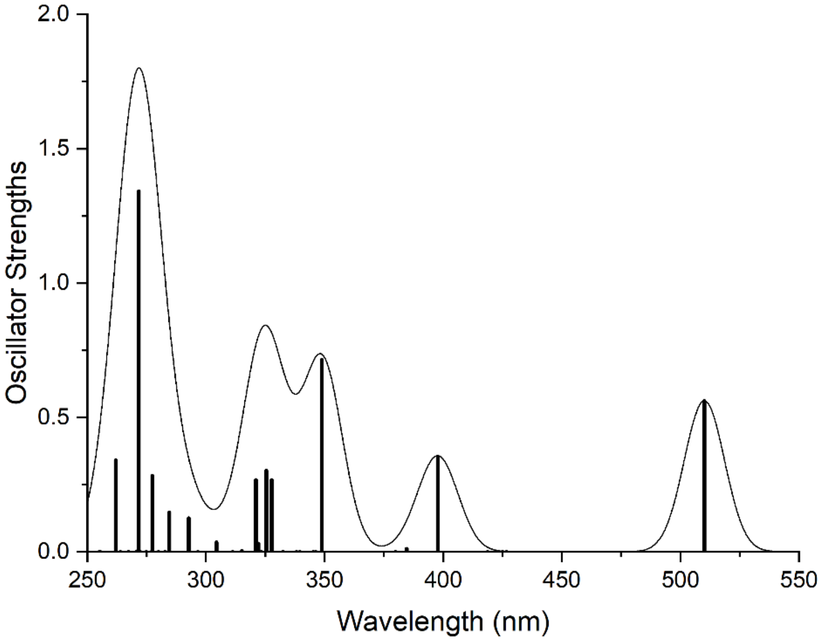

Figure S32. Calculated absorption spectrum of **8** with the oscillator strengths at the B3LYP-D3(BJ)/def2-TZVP (CPCM, CH_2Cl_2) level of theory.

7. References

1. R. K. Harris, E. D. Becker, S. M. C. d. Menezes, R. Goodfellow and P. Granger, *Pure Appl. Chem.*, 2001, **73**, 1795–1818.
2. P. Hindenberg, M. Busch, A. Paul, M. Bernhardt, P. Gemessy, F. Rominger and C. Romero-Nieto, *Angew. Chem. Int. Ed.*, 2018, **57**, 15157–15161.
3. A. Espineira-Gutierrez, I. Caro-Noakes, M. Zhang, M. Mas-Torrent, E. Regulska and C. Romero-Nieto, *Chem. Commun.*, 2025, **61**, 15590–15593.
4. L. Krause, R. Herbst-Irmer, G. M. Sheldrick and D. Stalke, *J. Appl. Crystallogr.*, 2015, **48**, 3–10.
5. G. Sheldrick, *Acta Crystallogr. A*, 2015, **71**, 3–8.
6. G. Sheldrick, *Acta Crystallogr. C*, 2015, **71**, 3–8.
7. P. Müller, *Crystallogr. Rev.*, 2009, **15**, 57–83.
8. O. V. Dolomanov, L. J. Bourhis, R. J. Gildea, J. A. K. Howard and H. Puschmann, *J. Appl. Crystallogr.*, 2009, **42**, 339–341.
9. D. Kratzert, J. J. Holstein and I. Krossing, *J. Appl. Crystallogr.*, 2015, **48**, 933–938.
10. F. Neese, *Wiley Interdiscip. Rev. Comput. Mol. Sci.*, 2012, **2**, 73–78.
11. F. Neese, *Wiley Interdiscip. Rev. Comput. Mol. Sci.*, 2022, **12**, e1606.
12. S. Grimme, J. Antony, S. Ehrlich and H. Krieg, *J. Chem. Phys.*, 2010, **132**.
13. A. D. Becke, *Phys. Rev. A*, 1988, **38**, 3098–3100.
14. A. D. Becke, *J. Chem. Phys.*, 1993, **98**, 5648–5652.
15. V. Barone and M. Cossi, *J. Phys. Chem. A*, 1998, **102**, 1995–2001.
16. F. Weigend and R. Ahlrichs, *Phys. Chem. Chem. Phys.*, 2005, **7**, 3297–3305.
17. M. K. Bogdos and B. Morandi, *J. Chem. Educ.*, 2023, **100**, 3641-3644.